THE JOURNAL OF PHYSICAL CHEMISTRY C
A JOURNAL OF THE AMERICAN CHEMICAL SOCIETY

pubs.acs.org/JPCC

Article

Electrocatalysis at Individual Colloidal Nanoparticles: A Quantitative Survey of Four Geometries via Electrochemical Cell Microscopy

Published as part of The Journal of Physical Chemistry virtual special issue "Early-Career and Emerging Researchers in Physical Chemistry Volume 2".

Partha Saha, Md. Maksudur Rahman, and Caleb M. Hill*

Cite This: *J. Phys. Chem. C* 2023, 127, 9059–9066

Read Online

ACCESS | Metrics & More | Article Recommendations | Supporting Information

ABSTRACT: Colloidal nanoparticles are inherently heterogeneous, exhibiting variations in size, shape, or composition that will impact their catalytic behavior. Understanding these particle-to-particle variations in catalytic behavior will be critical to realizing more stable, selective, and efficient catalyst systems, but it remains difficult to generate this understanding using conventional characterization techniques. Here, we demonstrate how targeted electrochemical cell microscopy (TECCM) can be utilized to rigorously evaluate the electrocatalytic behavior of hundreds of individual metal nanoparticle catalysts, enabling statistically meaningful insights into these systems to be generated. The electrocatalytic oxidation of hydrazine was studied in a series of Au nanoparticle systems (nanorods, nanospheres, triangular nanoprisms, and nanocubes), directly revealing particle-to-particle variations in key kinetic parameters and catalyst stability. On average, "sharper" nanoparticle geometries were found to exhibit higher initial activities but quickly degraded upon potential cycling. Interestingly, our single particle studies also reveal that while the smoother nanorod and nanosphere geometries exhibit stable behavior in an ensemble sense, this is in fact due to a complicated balance of populations which exhibit increasing or decreasing catalytic behavior over typical experimental time scales. Results from correlated optical spectroscopy and electron microscopy experiments suggest that these observed changes in catalytic behavior are not associated with significant changes in particle structure. Together, these results demonstrate the extensive heterogeneity present in common colloidal nanoparticle systems and the utility of single particle analytical techniques for studying these systems.

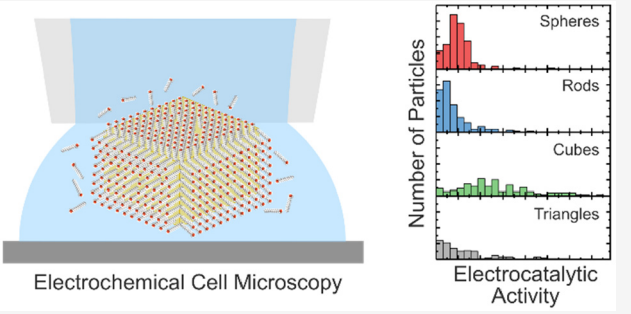

INTRODUCTION

Metal nanoparticles are a ubiquitous class of materials with important applications in catalysis,[1,2] energy conversion,[3,4] medicine,[5,6] and sensing.[7,8] Advancements in nanoparticle synthesis techniques have enabled many materials to be produced as nanoparticles in a variety of shapes and sizes, providing a promising route to controlling the physical and/or chemical properties of a material for a specific application. Unfortunately, these systems are inherently heterogeneous, exhibiting variations in size, shape, composition, surface functionality, etc., that can complicate fundamental studies into how a nanoparticle's properties are related to its structure. Simply put, there is no guarantee that the average structure of a heterogeneous system accurately reflects its macroscopic behavior. This is especially true in applications such as catalysis, where small changes in adsorption energies can lead to exponential changes in reaction rates.

Clearly resolving the heterogeneity present in nanostructured systems would thus be of massive benefit, as it would allow well-performing structures to be clearly identified and targeted for future synthetic efforts.[9] This has motivated a substantial amount of work over the past decade on the development and implementation of new analytical methods capable of measuring reaction rates at individual, nanoscale entities. Particularly impressive progress toward these goals has been made within the electrochemical community, where a variety of approaches have been demonstrated. Optical techniques such as dark field scattering,[10−13] fluorescence,[14−17] holography,[18] or interference[19] have been proven capable of probing discrete nanoparticles in a high-throughput fashion but are somewhat limited in terms of applicability. Direct electrochemical measurements are more attractive in this regard. The analysis of single nanoparticles using scanning

Received: March 1, 2023
Revised: April 18, 2023
Published: May 3, 2023

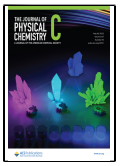

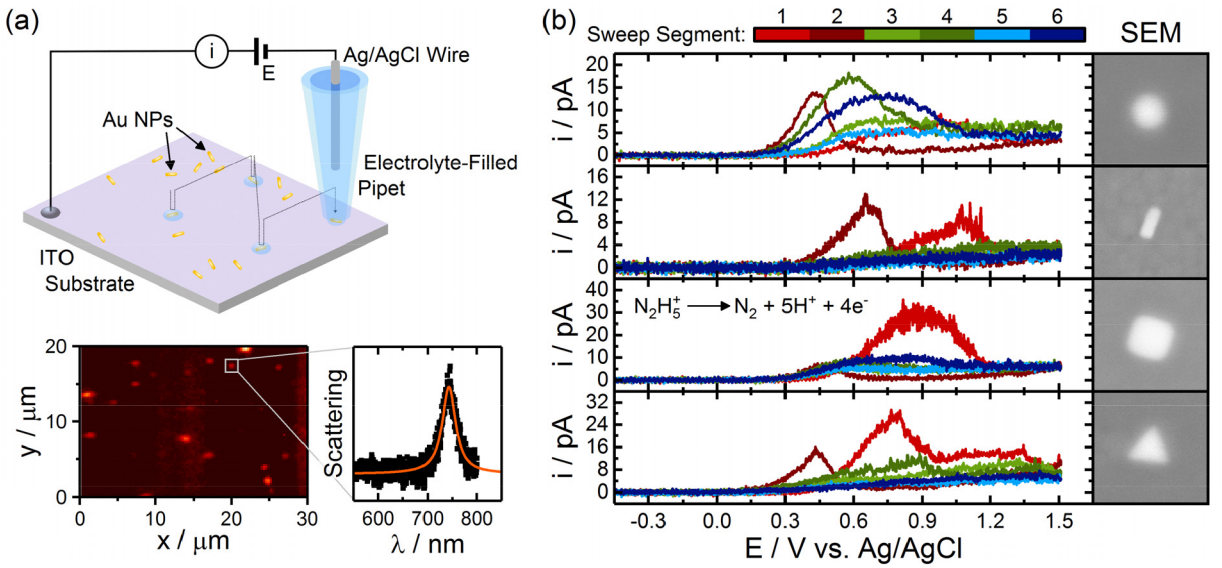

Figure 1. Probing the electrochemical properties of individual nanoparticles via TECCM. (a) General TECCM schematic. Individual nanoparticles dispersed across an ITO electrode are trapped within the meniscus of an electrolyte-filled pipet in a targeted fashion. Electrochemical currents flowing through the resulting microscopic cells reflect the catalytic properties of each individual nanoparticle. The bottom panel shows an example hyperspectral optical image of a typical sample and a scattering spectrum of an individual nanoparticle fit to a Lorentzian function. (b) Typical TECCM data recorded at individual Au nanoparticles. Cyclic voltammograms (1000 mV s^{-1} sweep rate) are shown for different particle shapes obtained with an ~1 μm pipet filled with an aqueous solution of 2 mM N_2H_4, 25 mM trisodium citrate, and 25 mM citric acid. Correlated SEM images of the same nanoparticles are also provided (200 nm × 200 nm).

electrochemical microscopy (SECM),[20−27] which employs an inlaid-disk electrode to probe reaction products in the vicinity of a sample, has been enabled through advancements in the fabrication of nanometer-scale probes. More recently, scanning electrochemical cell microscopy (SECCM), which utilizes electrolyte-filled pipets as electrochemical probes, has emerged as a powerful tool for studying a variety of electrochemical processes at individual nanostructures, including electrocatalysis,[28−35] ion transport,[36] corrosion,[37,38] photoelectrochemistry,[39−44] and electrodeposition.[45,46] Both SECM and SECCM following scanning-based protocols which are capable of producing detailed images revealing spatial variations in reactivity across an electrode but can be severely limited in terms of sample throughput.

Recently, our group demonstrated targeted electrochemical cell microscopy (TECCM) as a high-throughput approach toward the electrochemical characterization of individual nanostructures.[47−50] In TECCM, optical microscopy is utilized to quickly locate structures of interest in an electrode surface, enabling SECCM-type measurements to be performed in a targeted, high-throughput fashion. Using TECCM, it is feasible to characterize the electrochemical properties of hundreds of individual nanoparticles within realistic time scales, enabling the heterogeneity in these systems to be directly explored in a statistically meaningful manner not possible using other techniques. Here, we describe studies applying TECCM to systematically characterize the electrocatalytic properties of common shape-controlled Au nanoparticle systems. The results from these studies provide valuable new insights into how catalytic behavior varies at the single entity level in these ubiquitous systems, particularly with respect to catalyst stability.

METHODS

Nanoparticle Synthesis and Characterization. Au nanoparticles were synthesized following well-established colloidal syntheses.[51−54] The resulting nanoparticle suspensions were characterized via UV−vis spectrophotometry (Shimadzu 1650) and transmission electron microscopy (FEI Technai F20). Detailed synthesis procedures and characterization data for each particle geometry are provided in the Supporting Information.

Sample Preparation. 100 μL of the resulting nanoparticle dispersions was diluted with 900 μL of DI H_2O in a 1 mL centrifuge tube and centrifuged at 11000 *g* for 5 min at 30 °C. 900 μL of the resulting supernatant was then replaced with DI H_2O. This solution was again centrifuged at 11000 *g* and 30 °C for 5 min and 900 μL of the resulting supernatant replaced with DI H_2O. 5 μL of this cleaned nanoparticle dispersion was then drop-coated on ITO-coated cover glass slides (SPI, #1, 15−30 Ω/□) followed by UV/O_3 cleaning for 30 min (Novascan PSD-UV4).

Targeted Electrochemical Cell Microscopy Measurements. Single particle electrochemical measurements were performed using targeted electrochemical cell microscopy (TECCM) as described in detail by our group elsewhere.[47−50] In brief, the prepared nanoparticle samples were mounted onto a three-axis piezo stage (ThorLabs NanoMax) on an inverted optical microscope. Samples were illuminated by a white light source (Energetiq EQ-99, ~50 W cm^{-2}) at a 50° angle of incidence. Scattered light from the sample was collected by a long working distance microscope objective (Olympus, 50×, NA = 0.5) and directed onto the slit of a spectrometer/CCD (Andor Newton DU970-P/Shamrock SR-303i) through an achromatic relay lens assembly. Hyperspectral images of the samples were constructed by collecting a series of CCD images while translating the sample along one axis.

https://doi.org/10.1021/acs.jpcc.3c01427
J. Phys. Chem. C 2023, 127, 9059−9066

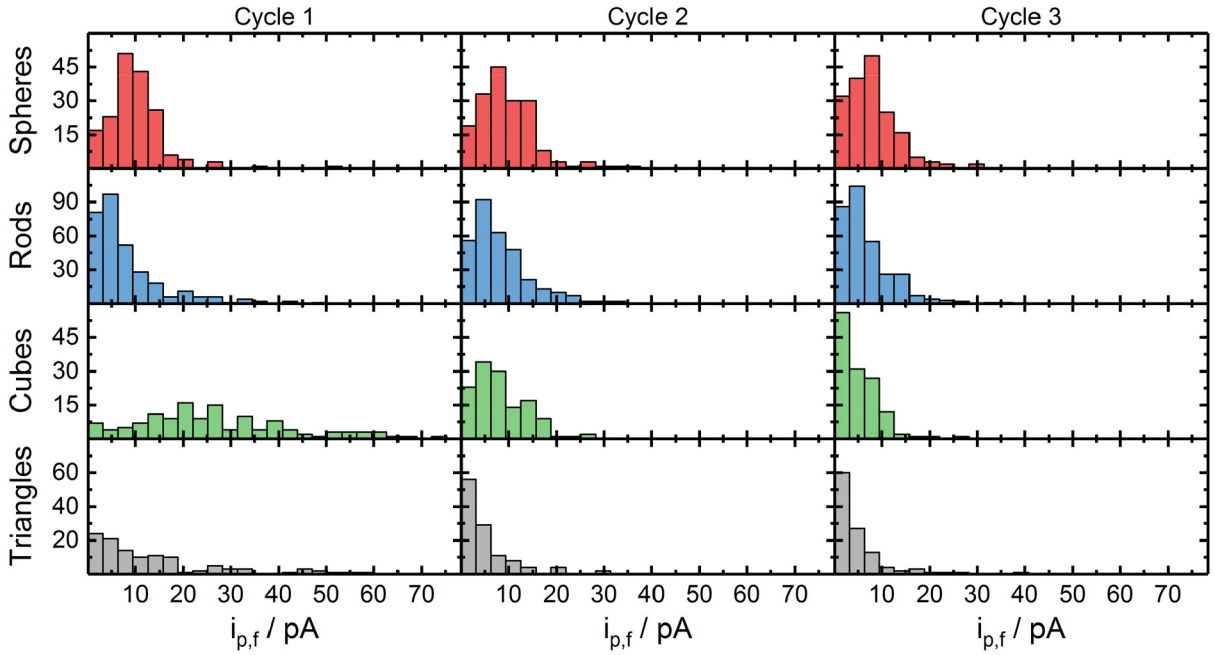

Figure 2. Statistical distribution of peak hydrazine oxidation currents (anodic sweep) measured at individual Au nanoparticles of varying geometry. Data taken from experiments performed as described in Figure 1.

Electrochemical measurements were performed using electrolyte-filled borosilicate pipets. The pipets were prepared from a borosilicate capillary using a pipet puller (Sutter P-2000, HEAT = 375, FIL = 4, VEL = 30, DEL = 200, PULL= 0). The probes were characterized using SEM, and the average size of these probes was found to be ca. 1 μm. Each pipet was then filled with electrolyte and a Ag/AgCl wire was inserted into the backside of the pipet to serve as a counter/reference electrode. The completed probe was then mounted onto another 3-axis translation stage (Physik Instrumente P-611.3S).

To carry out TECCM measurements, a hyperspectral image of the sample surface was first acquired. Individual nanoparticles were identified as diffraction-limited spots in the resulting optical image. The pipet probe was then brought into contact with the sample over each nanoparticle in a sequential fashion. A potential bias between the sample surface and the Ag/AgCl counter/reference electrode was applied during pipet approach over each nanoparticle, and probe−sample contact was detected as a sudden spike of current flowing through the now complete cell. Electrochemical measurements were performed in a two-electrode configuration using a patch-clamp amplifier (Dagan CHEM-CLAMP). Once contact was established, cyclic voltammograms were obtained by applying a triangular potential waveform to the sample and recording the current flowing through the cell. The pipet was then retracted and moved to a new nanoparticle where this cycle was repeated. All instrumentation was controlled using custom LabVIEW software. All cyclic voltammograms presented here were background corrected by subtracting the response recorded at a bare region of the ITO substrate. TECCM responses recorded at bare regions of the ITO substrates employed were very consistent and did not exhibit significant Faradaic responses (see Figure S4).

***In Situ* Optical Spectroscopy Studies.** In some experiments, optical spectra were recorded during electrochemical cycling. In these experiments, samples were aligned such that the position of a nanoparticle of interest was centered over the slit of the spectrometer. A large (~10 μm) diameter probe was then brought into contact with the sample over the particle of interest. The larger diameter was necessary in order to prevent excessive optical interference from the probe. Cyclic voltammograms were then obtained as described above, during which CCD images were continuously acquired.

RESULTS AND DISCUSSION

The basic experimental approach employed in these studies is illustrated in Figure 1a. Samples were prepared by drop-coating synthesized nanoparticle colloids onto an ITO substrate. The concentration of nanoparticles within these samples was adjusted to be ~0.1 μm^2 by controlling the concentration of the colloid solutions. Ligands on the surface of the nanoparticles were removed by cleaning the colloidal suspensions via centrifugation and subjecting the resulting samples to UV/O_3 cleaning.

TECCM was employed to characterize the electrochemical properties of individual nanoparticles within the prepared samples. In TECCM, optical images of a sample are first acquired to reveal the location of nanoparticles on the substrate surface. Here, dark field scattering was employed, which allowed individual Au nanoparticles to be identified on the basis of their strong surface plasmon resonance.[55,56] Individual nanoparticles appear as diffraction-limited spots in the resulting images and display sharp resonances in the resulting optical spectra. An electrolyte-filled pipet with terminal dimensions of ~1 μm was then brought into contact with the sample at each location, creating a miniaturized electrochemical cell. By applying a potential waveform between the ITO substrate and a Ag/AgCl wire immersed in the pipet, voltammetry can be performed reflecting the local properties of the electrode interface. Here, the pipet was filled with an aqueous solution consisting of N_2H_4 in a citrate buffer. As the ITO substrate employed is a poor catalyst for hydrazine oxidation ($N_2H_5^+ \rightarrow N_2 + 5H^+ + 4e^-$), the measured currents

https://doi.org/10.1021/acs.jpcc.3c01427
J. Phys. Chem. C 2023, 127, 9059−9066

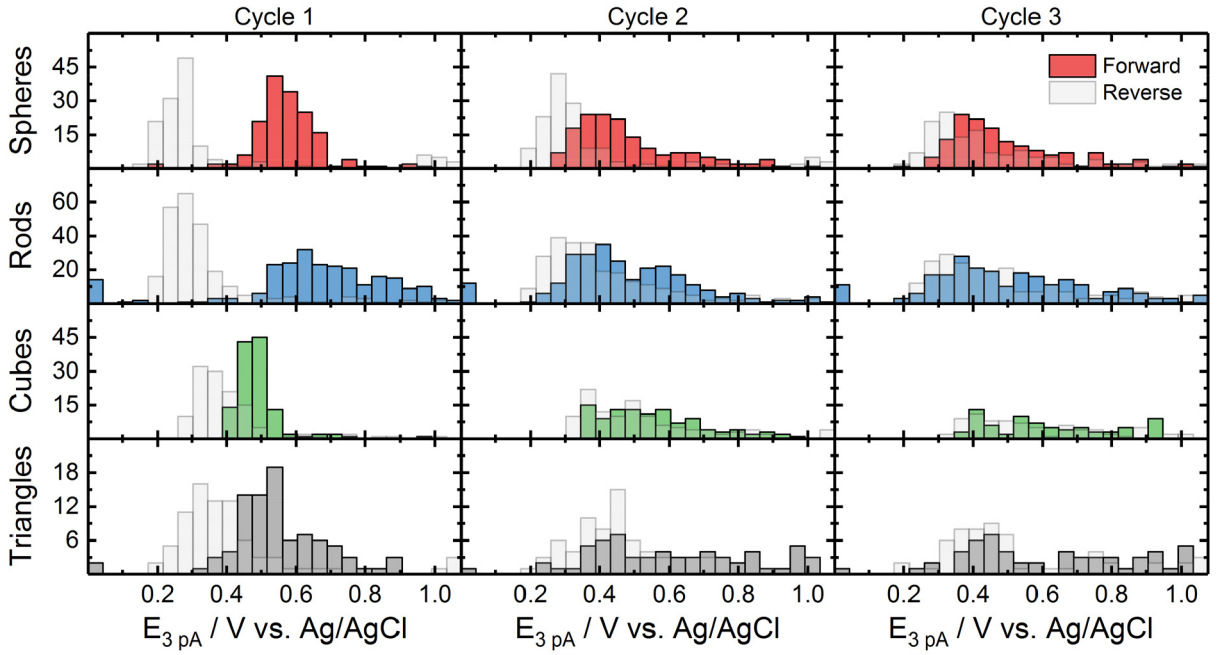

Figure 3. Statistical distribution of anodic onset potentials measured at individual Au nanoparticles of varying geometry. Data taken from experiments performed as described in Figure 1. Onset potentials here are defined as the most cathodic potential where an anodic current of 3 pA was observed. Data for forward (anodic) and reverse (cathodic) sweeps are provided.

reflect the local electrocatalytic rates at individual Au nanoparticles "trapped" within the microscopic cell created via TECCM.

Representative cyclic voltammograms obtained at individual Au nanospheres, nanorods, nanocubes, and triangular nanoprisms using TECCM are presented in Figure 1b. Correlated SEM imaging was performed to verify the presented measurements were obtained at individual nanoparticles. Two features are generally present in the presented voltammograms: (1) in the anodic sweep, an anodic peak is observed between 0.6 and 1.0 V vs Ag/AgCl, and (2) in the cathodic sweep, another anodic peak is observed between 0.3 and 0.8 V vs Ag/AgCl. Both features are attributable to electrocatalytic hydrazine oxidation. The complicated behavior results from oxide formation on the Au as detailed in previous reports.[48,57−59] In brief, oxide formation at potentials greater than 1.0 V vs Ag/AgCl decreases the electrocatalytic activity of the Au surface, resulting in a decrease in the observed currents. Oxide reduction at potentials between 0.6 and 0.7 V vs Ag/AgCl restores catalytic activity, resulting in another anodic peak.

It is clear from the voltammograms presented in Figure 1b that while the same general features are present, the electrochemical behavior of the investigated nanoparticles varies greatly at the single particle level. Some particles, such as the nanosphere in this example, exhibit relatively stable, even improving behavior during potential cycling, while others rapidly deactivate over time. There are also significant variations in the magnitude of currents observed between particles despite comparable surface areas. For reference, averaged responses observed at each nanoparticle geometry are provided in Figure S6.

In order to draw more meaningful conclusions regarding the behavior of these nanoparticle systems, a large number of similar experiments were performed to obtain data for hundreds of individual nanoparticles of each geometry. The resulting data were then analyzed to generate parameters describing the performance of each particle. The parameters chosen for analysis in these studies were the peak hydrazine oxidation current ($i_{p,f}$), onset potential (E_{3pA}), and Tafel slope. Details on the definition of each parameter and its experimental determination are provided in Figure S2 and the accompanying text in the Supporting Information. Statistical distributions for $i_{p,f}$ are summarized in Figure 2 for each particle geometry investigated. Histograms are presented for three successive potential cycles, enabling the evolution of catalyst behavior over time to be visualized. A few conclusions can be readily drawn from this data. First, it is clear that the peak currents observed vary widely within each geometry, exhibiting standard deviations comparable in magnitude to the average peak current values. Second, it is apparent that the "smooth" particle geometries, nanospheres, and nanorods exhibit relatively stable distributions over time, whereas the nanocubes and nanotriangles appear to lose significant catalytic activity between the first and second cycles. As will be discussed below, this second point is somewhat misleading in its implication that the nanospheres and nanorods exhibit "stable" electrocatalytic behavior.

An analysis of the onset potentials, E_{3pA}, defined as the most cathodic potential where a current of 3 pA was observed, is presented in Figure 3. Potentials for both the forward (anodic) and reverse (cathodic) sweeps are presented. Here, similar behavior is observed for the nanospheres and nanorods in which the onset potentials in the forward sweep shift to more cathodic potentials after the first cycle, a shift which may reflect cleaning and/or restructuring of the nanoparticle surface which improves hydrazine oxidation kinetics. The nanocubes and nanotriangles, on the other hand, exhibit anodic shifts in forward onset potentials, reflecting a tendency to quickly lose catalytic activity. For all particle geometries, differences between the forward and reverse onset potentials noticeably decrease between the first and second cycles, which shows that

https://doi.org/10.1021/acs.jpcc.3c01427
J. Phys. Chem. C 2023, 127, 9059−9066

the largest changes in behavior occur during one oxide formation/reduction cycle. The observed onset potentials are strongly correlated to the peak currents discussed above, as both are heavily influenced by the kinetic properties of each particle (see Figure S5). The Tafel slope at each particle was also determined through fitting each voltammogram in the vicinity of the onset potential as described in the Supporting Information. This data, which is presented in Figure S3, suggests that while distributions are similar between the different particle geometries, there could be significant particle-to-particle variations in the dominant reaction pathway.

While the data presented above illustrates the heterogeneity present in nanoparticle electrocatalyst systems, it does not describe the stability of these systems in a single particle sense. That is, while these simple histograms exhibit shifts over time, it is not clear to what fraction of particles are increasing, decreasing, or maintaining catalytic activity. To address this point, the peak hydrazine oxidation currents observed at each particle were analyzed by fitting to a simple exponential expression, $i_{p,f} = i^0_{p,f}e^{k_{ev}(N-1)}$. Here, $i^0_{p,f}$ represents the peak current during the first cycle, N represents the cycle number, and k_{ev} is a constant that describes how the system evolves over each successive cycle. $k_{ev} > 1$ implies the particle exhibits increasing currents, while $k_{ev} < 1$ would correspond to a particle exhibiting decreasing currents. Results from this analysis are presented in Figure 4a. Here, the nanocubes and nanotriangles, which both appeared to rapidly lose activity based on the data presented in Figure 2, exhibit distributions centered around a k_{ev} of ca. −1. Thus, these sharper shapes exhibit rather uniform behavior, with a majority of particles rapidly losing activity over time. The smoother nanosphere and nanorod geometries behave quite differently. Here, the k_{ev} distributions are centered around a value of 0 but vary between ca. −1 and 1. Example voltammograms recorded at nanorods with positive, negative, and roughly zero k_{ev} values are provided in Figure 4b to illustrate this variation. These results show that the apparent electrocatalytic stability of the nanosphere and nanorod geometries illustrated in Figure 2, which reflects what would be observed in a traditional, bulk electrochemistry experiment, is actually due to a complex, dynamic balance between populations of nanoparticles that are activating and deactivating over time. The k_{ev} values observed show a weak correlation with the initial peak oxidation currents, with larger k_{ev} values corresponding to lower initial currents (Figure 4c).

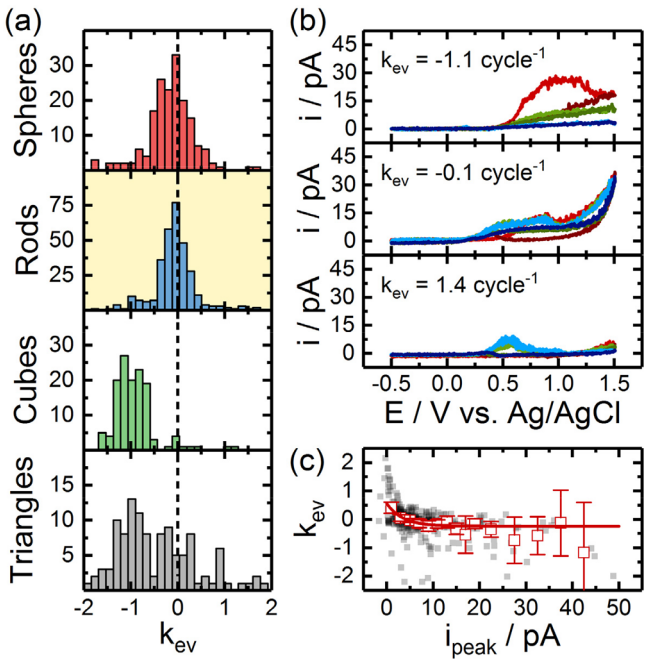

Figure 4. Statistical analysis of Au nanoparticle catalyst stability. (a) Distribution of k_{ev} for Au nanoparticles of different shapes. k_{ev} describes the evolution of peak hydrazine oxidation currents following $i_{peak} = i^0_{peak}e^{k_{ev}(N-1)}$, where N is the cycle number and i^0_{peak} is the peak oxidation current observed in the first anodic sweep. (b) Example voltammograms recorded at individual Au nanorods exhibiting different k_{ev} values. (c) Statistical relationship between k_{ev} and initial peak oxidation currents. Gray data points represent raw data, and red data points represent binned data with 95% confidence intervals indicated. All data were generated from experiments performed as described in Figure 1.

Correlated optical spectroscopy and electron microscopy experiments were performed in order to elucidate the origin of the rapid deactivation of the sharper Au nanoparticle geometries observed above. Results from experiments performed on Au nanocubes are provided in Figure 5. First, *in situ* dark field spectroscopy experiments were performed to track changes in an individual nanocube's plasmon resonance during potential cycling. As plasmon resonances are sensitive to changes in a particle's structure, local chemical environment, or even electron density, they can serve as sensitive indicators of structural changes during electrochemical cycling.[60−62] Figure 5a summarizes the results of a typical *in situ* spectroscopy experiment. Two important features can be observed in the optical data, summarized here as the peak scattering wavelength (λ_{max}). During the initial anodic sweep, a sudden blue-shift in λ_{max} can be observed at a potential of ∼0 V vs Ag/AgCl. A small anodic current wave is observed at the same potential. A likely origin of this feature is the desorption of positively charged ligands (cetyltrimethylammonium ions) remaining on the nanoparticle's surface, which would lower the effective refractive index in the vicinity of the nanoparticle and thus give rise to a blue-shift in λ_{max}. The sensitivity of λ_{max} to the refractive index of the surrounding medium is illustrated in Figure 5b, which gives simulated optical scattering spectra for a 60 nm edge length Au nanocube. The only other notable feature in the optical response is a gradual, reversible shift in λ_{max} which mirrors the applied potential. This shift, which arises from changes in the electron density within the particle, has been well documented elsewhere.[60,63−65]

Correlated electron microscopy studies were also performed to check for subtle structural changes occurring during potential cycling. Here, nanoparticles were dispersed onto a C-film TEM grid, and imaging was performed before and after similar potential cycling experiments. Representative images are displayed in Figure 5c. We were unable to observe any significant structural changes resulting from potential cycling under the conditions described here. Together, these results suggest that the rapid loss in catalytic activity observed at individual Au nanocubes in these studies arises from changes in the number of active sub-nm scale catalyst sites on the particle surface, not changes in particle morphology. Such changes are known to occur in nanostructured Au catalysts, particularly under optical illumination.[66,67]

https://doi.org/10.1021/acs.jpcc.3c01427
J. Phys. Chem. C 2023, 127, 9059−9066

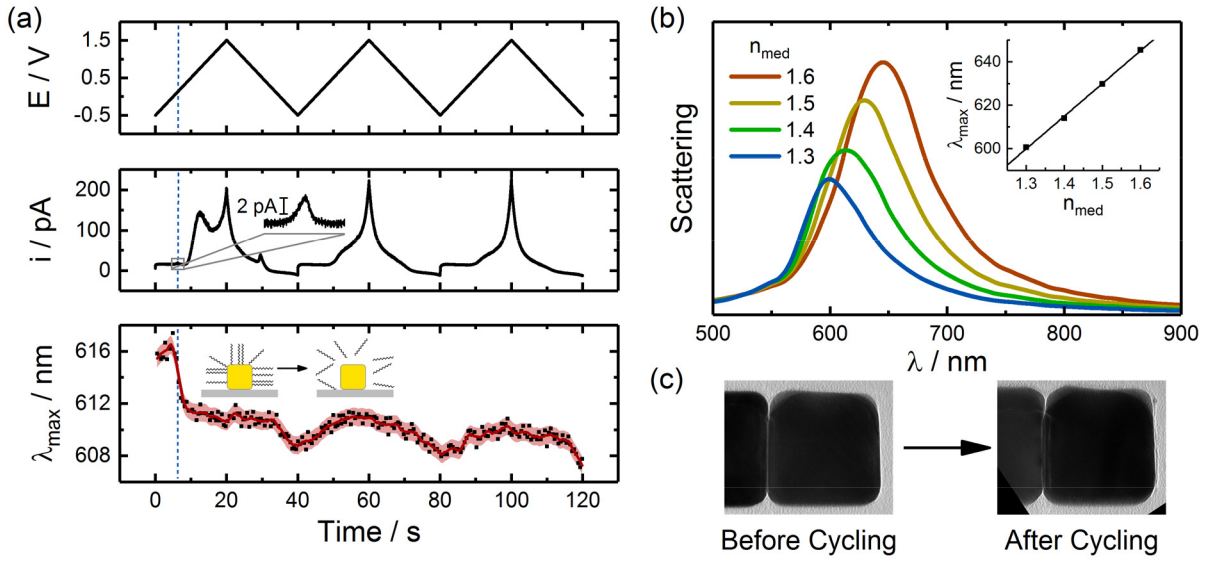

Figure 5. Correlated optical spectroscopy and electron microscopy studies of nanoparticle stability. (a) Results from *in situ* optical scattering studies of an individual Au nanocube during potential cycling (100 mV s^{-1}) on ITO. The top, middle, and bottom panels depict the applied potential waveform, the recorded current, and the peak scattering wavelength (λ_{max}), respectively. (b) Simulated optical scattering spectra for an individual Au nanocube (60 nm edge length) supported on ITO with varying medium refractive indices. Further details on the optical simulations can be found in the Supporting Information. (c) Transmission electron microscopy images of a Au nanocube dimer before and after electrochemical cycling on a C-film TEM grid.

CONCLUSIONS

In this report, TECCM was applied to systematically characterize the electrocatalytic activity of colloidal Au nanoparticle systems toward hydrazine oxidation. The high throughput afforded by TECCM enabled hundreds of individual nanoparticles of differing geometry to be rigorously characterized, allowing statistically meaningful insights into the heterogeneity of these systems to be generated. Large particle-to-particle variations in peak catalytic currents and onset potentials were observed, with sharper nanoparticle geometries (cubes and triangular prisms) exhibiting rapid losses in catalytic activity. Importantly, a thorough analysis of catalytic stability also revealed that the apparent stability of smoother geometries (spheres and rods) is actually due to a complex, dynamic balance between particles that exhibit increasing or decreasing catalytic activity over time. Correlated spectroscopic and microscopy studies did not find evidence of any significant morphological changes occurring in these catalyst systems during operation, suggesting changes in catalytic behavior are associated with changes in the availability of active catalyst sites on the particle surface due to adsorbates and/or surface restructuring. Together, these results present a valuable new view into the heterogeneous behavior of a ubiquitous class of nanostructured materials and highlight the need for single entity studies to reveal the complex dynamics which exist within these systems.

ASSOCIATED CONTENT

Supporting Information

The Supporting Information is available free of charge at https://pubs.acs.org/doi/10.1021/acs.jpcc.3c01427.

Nanoparticle synthesis procedures, additional experimental data, and details on finite element simulations (PDF)

AUTHOR INFORMATION

Corresponding Author

Caleb M. Hill − *Department of Chemistry, University of Wyoming, Laramie, Wyoming 82071, United States;* orcid.org/0000-0003-1989-3198; Email: caleb.hill@uwyo.edu

Authors

Partha Saha − *Department of Chemistry, University of Wyoming, Laramie, Wyoming 82071, United States;* orcid.org/0000-0002-4307-9287

Md. Maksudur Rahman − *Department of Chemistry, University of Wyoming, Laramie, Wyoming 82071, United States;* orcid.org/0000-0002-3545-151X

Complete contact information is available at: https://pubs.acs.org/10.1021/acs.jpcc.3c01427

Notes

The authors declare no competing financial interest.

ACKNOWLEDGMENTS

The authors acknowledge generous support for this work from the National Science Foundation (CHE-2045593) and the University of Wyoming School of Energy Resources.

ABBREVIATIONS

SECM, scanning electrochemical microscopy; SECCM, scanning electrochemical cell microscopy; SEM, scanning electron microscopy; TEM, transmission electron microscopy; ITO, indium tin oxide.

REFERENCES

(1) Ishida, T.; Murayama, T.; Taketoshi, A.; Haruta, M. Importance of Size and Contact Structure of Gold Nanoparticles for the Genesis of Unique Catalytic Processes. *Chem. Rev.* **2020**, *120* (2), 464−525.

(2) Daniel, M. C.; Astruc, D. Gold Nanoparticles: Assembly, Supramolecular Chemistry, Quantum-Size-Related Properties, and Applications toward Biology, Catalysis, and Nanotechnology. *Chem. Rev.* **2004**, *104* (1), 293−346.
(3) Coowar, F. A.; Vitins, G.; Mepsted, G. O.; Waring, S. C.; Horsfall, J. A. Electrochemical Oxidation of Borohydride at Nano-Gold-Based Electrodes: Application in Direct Borohydride Fuel Cells. *J. Power Sources* **2008**, *175* (1), 317−324.
(4) Pasta, M.; Hu, L.; La Mantia, F.; Cui, Y. Electrodeposited Gold Nanoparticles on Carbon Nanotube-Textile: Anode Material for Glucose Alkaline Fuel Cells. *Electrochem. commun.* **2012**, *19*, 81−84.
(5) Murphy, C. J.; Gole, A. M.; Stone, J. W.; Sisco, P. N.; Alkilany, A. M.; Goldsmith, E. C.; Baxter, S. C. Gold Nanoparticles in Biology: Beyond Toxicity to Cellular Imaging. *Acc. Chem. Res.* **2008**, *41* (12), 1721−1730.
(6) Giljohann, D. A.; Seferos, D. S.; Daniel, W. L.; Massich, M. D.; Patel, P. C.; Mirkin, C. A. Gold Nanoparticles for Biology and Medicine. *Angew. Chem., Int. Ed.* **2010**, *49* (19), 3280−3294.
(7) Qin, L.; Zeng, G.; Lai, C.; Huang, D.; Xu, P.; Zhang, C.; Cheng, M.; Liu, X.; Liu, S.; Li, B.; et al. Gold Rush" in Modern Science: Fabrication Strategies and Typical Advanced Applications of Gold Nanoparticles in Sensing. *Coord. Chem. Rev.* **2018**, *359*, 1−31.
(8) Saha, K.; Agasti, S. S.; Kim, C.; Li, X.; Rotello, V. M. Gold Nanoparticles in Chemical and Biological Sensing. *Chem. Rev.* **2012**, *112* (5), 2739−2779.
(9) Baker, L. A. Perspective and Prospectus on Single-Entity Electrochemistry. *J. Am. Chem. Soc.* **2018**, *140* (46), 15549−15559.
(10) Hill, C. M.; Pan, S. A Dark Field Scattering Spectroelectrochemical Technique for Tracking the Electrodeposition of Single Ag Nanoparticles. *J. Am. Chem. Soc.* **2013**, *135* (46), 17250−17253.
(11) Ma, Y.; Highsmith, A. L.; Hill, C. M.; Pan, S. Dark-Field Scattering Spectroelectrochemistry Analysis of Hydrazine Oxidation at Au Nanoparticle-Modified Transparent Electrodes. *J. Phys. Chem. C* **2018**, *122* (32), 18603−18614.
(12) Hill, C. M.; Bennett, R.; Zhou, C.; Street, S.; Zheng, J.; Pan, S. Single Ag Nanoparticle Spectroelectrochemistry via Dark-Field Scattering and Fluorescence Microscopies. *J. Phys. Chem. C* **2015**, *119* (12), 6760−6768.
(13) Wonner, K.; Evers, M. V.; Tschulik, K. Simultaneous Opto- and Spectro-Electrochemistry: Reactions of Individual Nanoparticles Uncovered by Dark-Field Microscopy. *J. Am. Chem. Soc.* **2018**, *140* (40), 12658−12661.
(14) Sambur, J. B.; Chen, P. Distinguishing Direct and Indirect Photoelectrocatalytic Oxidation Mechanisms Using Quantitative Single-Molecule Reaction Imaging and Photocurrent Measurements. *J. Phys. Chem. C* **2016**, *120* (37), 20668−20676.
(15) Sambur, J. B.; Chen, T. Y.; Choudhary, E.; Chen, G.; Nissen, E. J.; Thomas, E. M.; Zou, N.; Chen, P. Sub-Particle Reaction and Photocurrent Mapping to Optimize Catalyst-Modified Photoanodes. *Nature* **2016**, *530* (7588), 77−80.
(16) Zhou, X.; Xu, W.; Liu, G.; Panda, D.; Chen, P. Size-Dependent Catalytic Activity and Dynamics of Gold Nanoparticles at the Single-Molecule Level. *J. Am. Chem. Soc.* **2010**, *132* (1), 138−146.
(17) Zou, N.; Zhou, X.; Chen, G.; Andoy, N. M.; Jung, W.; Liu, G.; Chen, P. Cooperative Communication within and between Single Nanocatalysts. *Nat. Chem.* **2018**, *10* (6), 607−614.
(18) Brasiliense, V.; Berto, P.; Combellas, C.; Tessier, G.; Kanoufi, F. Electrochemistry of Single Nanodomains Revealed by Three-Dimensional Holographic Microscopy. *Acc. Chem. Res.* **2016**, *49*, 2049−2057.
(19) Valavanis, D.; Ciocci, P.; Meloni, G. N.; Morris, P.; Lemineur, J. F.; McPherson, I. J.; Kanoufi, F.; Unwin, P. R. Hybrid Scanning Electrochemical Cell Microscopy-Interference Reflection Microscopy (SECCM-IRM): Tracking Phase Formation on Surfaces in Small Volumes. *Faraday Discuss.* **2022**, *233*, 122−148.
(20) Askarova, G.; Hesari, M.; Wang, C.; Mirkin, M. V. Decoupling Through-Tip Illumination from Scanning in Nanoscale Photo-SECM. *Anal. Chem.* **2022**, *94* (20), 7169−7173.
(21) Sarkar, S.; Wang, X.; Hesari, M.; Chen, P.; Mirkin, M. V. Scanning Electrochemical and Photoelectrochemical Microscopy on Finder Grids: Toward Correlative Multitechnique Imaging of Surfaces. *Anal. Chem.* **2021**, *93* (13), 5377−5382.
(22) Blanchard, P. Y.; Sun, T.; Yu, Y.; Wei, Z.; Matsui, H.; Mirkin, M. V. Scanning Electrochemical Microscopy Study of Permeability of a Thiolated Aryl Multilayer and Imaging of Single Nanocubes Anchored to It. *Langmuir* **2016**, *32* (10), 2500−2508.
(23) Yu, Y.; Sun, T.; Mirkin, M. V. Scanning Electrochemical Microscopy of Single Spherical Nanoparticles: Theory and Particle Size Evaluation. *Anal. Chem.* **2015**, *87* (14), 7446−7453.
(24) Yu, Y.; Gao, Y.; Hu, K.; Blanchard, P. Y.; Noël, J. M.; Nareshkumar, T.; Phani, K. L.; Friedman, G.; Gogotsi, Y.; Mirkin, M. V. Electrochemistry and Electrocatalysis at Single Gold Nanoparticles Attached to Carbon Nanoelectrodes. *ChemElectroChem.* **2015**, *2* (1), 58−63.
(25) Sun, T.; Yu, Y.; Zacher, B. J.; Mirkin, M. V. Scanning Electrochemical Microscopy of Individual Catalytic Nanoparticles. *Angew. Chem., Int. Ed.* **2014**, *53* (51), 14120−14123.
(26) Kim, J.; Renault, C.; Nioradze, N.; Arroyo-Currás, N.; Leonard, K. C.; Bard, A. J. Electrocatalytic Activity of Individual Pt Nanoparticles Studied by Nanoscale Scanning Electrochemical Microscopy. *J. Am. Chem. Soc.* **2016**, *138* (27), 8560−8568.
(27) Hill, C. M.; Pan, S. SECM Techniques for Locally Interrogating the Photocatalytic Activity of Semiconducting Materials for Solar-Driven Chemical Transformations. *Scanning Electrochemical Microscopy* **2022**, 361−378.
(28) Siepser, N. P.; Choi, M. H.; Alden, S. E.; Baker, L. A. Single-Entity Electrocatalysis at Electrode Ensembles Prepared by Template Synthesis. *J. Electrochem. Soc.* **2021**, *168* (12), 126526.
(29) Choi, M.; Siepser, N. P.; Jeong, S.; Wang, Y.; Jagdale, G.; Ye, X.; Baker, L. A. Probing Single-Particle Electrocatalytic Activity at Facet-Controlled Gold Nanocrystals. *Nano Lett.* **2020**, *20* (2), 1233−1239.
(30) Alden, S. E.; Siepser, N. P.; Patterson, J. A.; Jagdale, G. S.; Choi, M.; Baker, L. A. Array Microcell Method (AMCM) for Serial Electroanalysis. *ChemElectroChem.* **2020**, *7* (5), 1084−1091.
(31) Jeong, S.; Choi, M. H.; Jagdale, G. S.; Zhong, Y.; Siepser, N. P.; Wang, Y.; Zhan, X.; Baker, L. A.; Ye, X. Unraveling the Structural Sensitivity of CO_2 Electroreduction at Facet-Defined Nanocrystals via Correlative Single-Entity and Macroelectrode Measurements. *J. Am. Chem. Soc.* **2022**, *144* (28), 12673−12680.
(32) Bentley, C. L.; Kang, M.; Unwin, P. R. Nanoscale Surface Structure−Activity in Electrochemistry and Electrocatalysis. *J. Am. Chem. Soc.* **2019**, *141* (6), 2179−2193.
(33) Bentley, C. L.; Kang, M.; Unwin, P. R. Nanoscale Structure Dynamics within Electrocatalytic Materials. *J. Am. Chem. Soc.* **2017**, *139* (46), 16813−16821.
(34) Kang, M.; Perry, D.; Bentley, C. L.; West, G.; Page, A.; Unwin, P. R. Simultaneous Topography and Reaction Flux Mapping at and around Electrocatalytic Nanoparticles. *ACS Nano* **2017**, *11* (9), 9525−9535.
(35) Li, M.; Ye, K. H.; Qiu, W.; Wang, Y.; Ren, H. Heterogeneity between and within Single Hematite Nanorods as Electrocatalysts for Oxygen Evolution Reaction. *J. Am. Chem. Soc.* **2022**, *144* (12), 5247−5252.
(36) Bentley, C. L.; Kang, M.; Bukola, S.; Creager, S. E.; Unwin, P. R. High-Resolution Ion-Flux Imaging of Proton Transport through Graphene|Nafion Membranes. *ACS Nano* **2022**, *16* (4), 5233−5245.
(37) Wang, Y.; Li, M.; Gordon, E.; Ye, Z.; Ren, H. Nanoscale Colocalized Electrochemical and Structural Mapping of Metal Dissolution Reaction. *Anal. Chem.* **2022**, *94* (25), 9058−9064.
(38) Li, M.; Wang, Y.; Blount, B.; Gordon, E.; Muñoz-Castañeda, J. A.; Ye, Z.; Ren, H. Stochastic Local Breakdown of Oxide Film on Ni from Identical-Location Imaging: One Single Site at a Time. *Nano Lett.* **2022**, *22* (15), 6313−6319.
(39) Hill, J. W.; Fu, Z.; Tian, J.; Hill, C. M. Locally Engineering and Interrogating the Photoelectrochemical Behavior of Defects in

https://doi.org/10.1021/acs.jpcc.3c01427
J. Phys. Chem. C 2023, 127, 9059−9066

Transition Metal Dichalcogenides. *J. Phys. Chem. C* **2020**, *124* (31), 17141−17149.
(40) Strange, L. E.; Yadav, J.; Garg, S.; Shinde, P. S.; Hill, J. W.; Hill, C. M.; Kung, P.; Pan, S. Investigating the Redox Properties of Two-Dimensional MoS_2 Using Photoluminescence Spectroelectrochemistry and Scanning Electrochemical Cell Microscopy. *J. Phys. Chem. Lett.* **2020**, *11* (9), 3488−3494.
(41) Hill, J. W.; Hill, C. M. Directly Mapping Photoelectrochemical Behavior within Individual Transition Metal Dichalcogenide Nanosheets. *Nano Lett.* **2019**, *19* (8), 5710−5716.
(42) Hill, J. W.; Hill, C. M. Directly Visualizing Carrier Transport and Recombination at Individual Defects within 2D Semiconductors. *Chem. Sci.* **2021**, *12* (14), 5102−5112.
(43) Tolbert, C. L.; Hill, C. M. Electrochemically Probing Exciton Transport in Monolayers of Two-Dimensional Semiconductors. *Faraday Discuss.* **2022**, *233*, 163−174.
(44) Tolbert, C. L.; McDonald, D. M.; Hill, C. M. Electrochemical Techniques for Visualizing Photoelectrochemical Processes at the Nanoscale. *Curr. Opin. Electrochem.* **2023**, *37*, 101164.
(45) Rahman, Md. M.; Tolbert, C. L.; Saha, P.; Halpern, J. M.; Hill, C. M. On-Demand Electrochemical Fabrication of Ordered Nanoparticle Arrays Using Scanning Electrochemical Cell Microscopy. *ACS Nano* **2022**, *16* (12), 21275−21282.
(46) Lai, S. C. S.; Lazenby, R. A.; Kirkman, P. M.; Unwin, P. R. Nucleation, Aggregative Growth and Detachment of Metal Nanoparticles during Electrodeposition at Electrode Surfaces. *Chem. Sci.* **2015**, *6* (2), 1126−1138.
(47) Saha, P.; Rahman, Md. M.; Hill, C. M. Borohydride Oxidation Electrocatalysis at Individual, Shape-Controlled Au Nanoparticles. *Electrochem. Sci. Adv.* **2022**, *2*, e2100120.
(48) Saha, P.; Hill, J. W.; Walmsley, J. D.; Hill, C. M. Probing Electrocatalysis at Individual Au Nanorods via Correlated Optical and Electrochemical Measurements. *Anal. Chem.* **2018**, *90* (21), 12832−12839.
(49) Walmsley, J. D.; Hill, J. W.; Saha, P.; Hill, C. M. Probing Electrocatalytic CO_2 Reduction at Individual Cu Nanostructures via Optically Targeted Electrochemical Cell Microscopy. *J. Anal. Test.* **2019**, *3* (2), 140−149.
(50) Maley, M.; Hill, J. W.; Saha, P.; Walmsley, J. D.; Hill, C. M. The Role of Heating in the Electrochemical Response of Plasmonic Nanostructures under Illumination. *J. Phys. Chem. C* **2019**, *123* (19), 12390−12399.
(51) Scarabelli, L.; Coronado-Puchau, M.; Giner-Casares, J. J.; Langer, J.; Liz-Marzán, L. M. Monodisperse Gold Nanotriangles: Size Control, Large-Scale Self-Assembly, and Performance in Surface-Enhanced Raman Scattering. *ACS Nano* **2014**, *8* (6), 5833−5842.
(52) Park, J.-E.; Lee, Y.; Nam, J. M. Precisely Shaped, Uniformly Formed Gold Nanocubes with Ultrahigh Reproducibility in Single-Particle Scattering and Surface-Enhanced Raman Scattering. *Nano Lett.* **2018**, *18* (10), 6475−6482.
(53) Hanske, C.; González-Rubio, G.; Hamon, C.; Formentín, P.; Modin, E.; Chuvilin, A.; Guerrero-Martínez, A.; Marsal, L. F.; Liz-Marzán, L. M. Large-Scale Plasmonic Pyramidal Supercrystals via Templated Self-Assembly of Monodisperse Gold Nanospheres. *J. Phys. Chem. C* **2017**, *121* (20), 10899−10906.
(54) Nikoobakht, B.; El-Sayed, M. A. Preparation and Growth Mechanism of Gold Nanorods (NRs) Using Seed-Mediated Growth Method. *Chem. Mater.* **2003**, *15* (10), 1957−1962.
(55) Mulvaney, P. Surface Plasmon Spectroscopy of Nanosized Metal Particles. *Langmuir* **1996**, *12* (3), 788−800.
(56) Willets, K. A.; van Duyne, R. P. Localized Surface Plasmon Resonance Spectroscopy and Sensing. *Annu. Rev. Phys. Chem.* **2007**, *58* (1), 267−297.
(57) Eisner, U.; Gileadi, E. Anodic Oxidation of Hydrazine and Its Derivatives. *J. Electroanal. Chem. Interfacial Electrochem.* **1970**, *28* (1), 81−92.
(58) Eisner, U.; Zemer, Y. Anodic Oxidation of Hydrazine and Its Derivatives. *J. Electroanal. Chem. Interfacial Electrochem.* **1972**, *38* (2), 381−388.
(59) Eisner, U.; Zommer, N. Anodic Oxidation of Hydrazine and Its Derivatives. *J. Electroanal. Chem. Interfacial Electrochem.* **1971**, *30* (3), 433−441.
(60) Byers, C. P.; Hoener, B. S.; Chang, W.-S.; Yorulmaz, M.; Link, S.; Landes, C. F. Single-Particle Spectroscopy Reveals Heterogeneity in Electrochemical Tuning of the Localized Surface Plasmon. *J. Phys. Chem. B* **2014**, *118* (49), 14047−14055.
(61) Llorente, V. B.; Dzhagan, V. M.; Gaponik, N.; Iglesias, R. A.; Zahn, D. R. T.; Lesnyak, V. Electrochemical Tuning of Localized Surface Plasmon Resonance in Copper Chalcogenide Nanocrystals. *J. Phys. Chem. C* **2017**, *121* (33), 18244−18253.
(62) Fang, Y.; Wang, W.; Wo, X.; Luo, Y.; Yin, S.; Wang, Y.; Shan, X.; Tao, N. Plasmonic Imaging of Electrochemical Oxidation of Single Nanoparticles. *J. Am. Chem. Soc.* **2014**, *136* (36), 12584−12587.
(63) Hoener, B. S.; Zhang, H.; Heiderscheit, T. S.; Kirchner, S. R.; de Silva Indrasekara, A. S.; Baiyasi, R.; Cai, Y.; Nordlander, P.; Link, S.; Landes, C. F.; et al. Spectral Response of Plasmonic Gold Nanoparticles to Capacitive Charging: Morphology Effects. *J. Phys. Chem. Lett.* **2017**, *8* (12), 2681−2688.
(64) Collins, S. S. E.; Wei, X.; McKenzie, T. G.; Funston, A. M.; Mulvaney, P. Single Gold Nanorod Charge Modulation in an Ion Gel Device. *Nano Lett.* **2016**, *16* (11), 6863−6869.
(65) Novo, C.; Funston, A. M.; Gooding, A. K.; Mulvaney, P. Electrochemical Charging of Single Gold Nanorods. *J. Am. Chem. Soc.* **2009**, *131* (41), 14664−14666.
(66) Wang, X.; Ye, Z.; Hua, J.; Wei, L.; Lin, S.; Xiao, L. Fast Surface Restructuring within the Gap of Au Nanocube Dimer for the Enhancement of Catalytic Efficiency. *CCS Chem.* **2022**, *4* (3), 1074−1086.
(67) Ye, Z.; Wei, L.; Xiao, L.; Wang, J. Laser Illumination-Induced Dramatic Catalytic Activity Change on Au Nanospheres. *Chem. Sci.* **2019**, *10* (22), 5793−5800.

https://doi.org/10.1021/acs.jpcc.3c01427
J. Phys. Chem. C 2023, 127, 9059−9066